AIAA 2006-374

44th AIAA Aerospace Sciences Meeting and Exhibit, 9-12 Jan 2006, Reno, Nevada

Effective Discharge Dynamics for Plasma Actuators

Subrata Roy[*], K.P. Singh[†] and Haribalan Kumar[‡]

Computational Plasma Dynamics Laboratory
Mechanical Engineering, Kettering University
Flint, MI 48504, USA

Datta V. Gaitonde[§] and Miguel Visbal[**]

Computational Sciences Branch
Air Force Research Laboratory
Wright Pat AFB, Ohio 45433, USA

Some effective control parameters for active separation mitigation using asymmetric dielectric barrier discharges is studied by considering the weakly ionized gas flow past a flat plate at angle of attack. A self-consistent plasma actuator model is employed to couple the electric force field to the momentum of the neutral gas. The equations governing the motion of electrons, ions and neutrals are solved with Poisson equation to study separation control for different parameters. It is observed that dielectric surface becomes negatively charged and a time averaged force acts on the plasma predominantly downstream, with a transverse component towards the wall. Momentum of the plasma couples to neutral gas through collisions, which results enhancement of near-wall momentum yielding a wall-jet-like feature that effectively eliminates the separation bubble. The impact of several physical and geometric parameters such as the amplitude and shape of excitation, dielectric constants, the initial ionization level, and the electrode shape is discussed. It is found that for an optimum distance between the exposed electrodes kept at a single phase the momentum transfer to the neighboring gas is cumulative showing, however, a diminishing return with increasing number of electrodes.

Nomenclature

A,B	Coefficients	Z	Ionization rate, /s
D	Diffusion coefficient, cm^2/s		
d	Characteristic length, cm	Subscripts:	
E	Electric field, V/cm	α	Species
e	Electron charge, coulomb	B	Bohm
ε	Permittivity, farad/m	e	Electron, finite element
F	Electric force density, dynes/cm^3, $\mu N/cm^3$	f	Fluid
ϕ	Potential, V	i	Ion
Γ	Flux, cm^{-2}/s	n	Neutral
I	Current, Amp/cm^2	0	Reference value
λ_{De}	Electron Debye length, χm		
λ_i	Ion mean free path, cm		
M	mass, kg		
μ	Mobility, $cm^2V^{-1}s^{-1}$		
n	Number density, cm^{-3}		
ω	Applied frequency, radians		
p	Pressure, Pa		
r	Recombination coefficient		
S	Ionization frequency, s^{-1}		
T	Temperature, eV		
t	Time coordinate, s		
u,**v**	Velocity, m/s		
x	Spatial coordinate, cm		

[*] Associate Professor of Mechanical Engineering, 1700 West Third Avenue, and AIAA Associate Fellow.
[†] Post Doctoral Research Associate of the CPDL, 1700 West Third Avenue.
[‡] Graduate Student of the CPDL, 1700 West Third Avenue, and AIAA Student Member.
[§] Technical Area Leader, Air Vehicles Directorate/VAAC, 2210 8th St., and AIAA Associate Fellow.
[**] Technical Area Leader, Air Vehicles Directorate/VAAC, 2210 8th St., and AIAA Associate Fellow.

Report Documentation Page

Form Approved
OMB No. 0704-0188

1. REPORT DATE	2. REPORT TYPE	3. DATES COVERED
JAN 2006		**00-00-2006 to 00-00-2006**

4. TITLE AND SUBTITLE	5a. CONTRACT NUMBER
Effective Discharge Dynamics for Plasma Actuators	5b. GRANT NUMBER
	5c. PROGRAM ELEMENT NUMBER
6. AUTHOR(S)	5d. PROJECT NUMBER
	5e. TASK NUMBER
	5f. WORK UNIT NUMBER
7. PERFORMING ORGANIZATION NAME(S) AND ADDRESS(ES) **Kettering University ,Computational Plasma Dynamics Laboratory,Department of Mechanical Engineering,Flint,MI,48504**	8. PERFORMING ORGANIZATION REPORT NUMBER
9. SPONSORING/MONITORING AGENCY NAME(S) AND ADDRESS(ES)	10. SPONSOR/MONITOR'S ACRONYM(S)
	11. SPONSOR/MONITOR'S REPORT NUMBER(S)

12. DISTRIBUTION/AVAILABILITY STATEMENT
Approved for public release; distribution unlimited

13. SUPPLEMENTARY NOTES

14. ABSTRACT

15. SUBJECT TERMS

16. SECURITY CLASSIFICATION OF:			17. LIMITATION OF ABSTRACT	18. NUMBER OF PAGES	19a. NAME OF RESPONSIBLE PERSON
a. REPORT	b. ABSTRACT	c. THIS PAGE			
unclassified	**unclassified**	**unclassified**	**Same as Report (SAR)**	**12**	

I. Introduction

FLOW control is useful for various aerospace applications. Specifically, efficient passive or active flow actuators are employed to mitigate performance deficiencies under off-design conditions where separation occur impairing performance.[1-4] Experimental observations have shown the capability of dielectric barrier devices, operating at relatively low power levels, to suppress separation in a wide range of applications even at atmospheric pressures[5,6]. These plasma-based actuators exhibit several potential benefits in active flow control applications, including absence of moving parts, rapid on-off deployment and attractive self-limiting characteristics. The discharge may be characterized as transient with a time scale of the order of a few microseconds while that for the bulk gas flow is in milliseconds. This allows the fluid to respond relatively instantaneously to the electrical inputs.

Recent studies have demonstrated the capability of plasma discharges to promote boundary layer attachment on airfoils at a high angle-of-attack. Plasma discharge accomplishes this by supplying additional body force to the boundary layer which remains effective even at atmospheric pressures. Acoustic testing of the dielectric barrier discharge (DBD) plasma actuator was done by Baird et al.[7]. Their results suggest that compressibility effects may play an important role in the momentum coupling between plasma and neutral gas. The use of plasma actuator for a variety of flow control applications and its design has also been studied[8]. Numerical simulations have been performed based on assumed body force per unit volume of plasma. Different empirical models for dependence of the volume of plasma on input voltage, frequency and electrode geometry have also been developed and used to further optimize actuator performance. The plasma composition, its physics of generation and methods of plasma momentum coupling to neutral gas have been studied[9] by particle-in-cell and Monte-Carlo (PIC-DSMC) methods. They found that ionization is not equal during both cycles which results in the asymmetrically arranged plasma actuator producing a net force in one direction. Similar result has also been demonstrated by using hydrodynamic first principles with drift diffusion approximation using a three-fluid (charge-neutral) system.[10] The body forces originating from radio-frequency driven asymmetric dielectric barrier-discharge actuators have been calculated using time-accurate unsteady direct numerical simulations[10,11] and the response of the flow past a stalled NACA 0015 airfoil at 15 deg angle of attack and Reynolds number of 45,000 have been found out.[11,12] Importantly, the mean and transient flow response in Ref. 13 show gradual purging of large scale features associated with separation due to the formation of a wall-jet as the actuator is placed slightly downstream of separation. The results suggest that both streamwise and normal (towards the wall) components play important roles. The unsteady mode directly associated with the forcing and vortex shedding occurring near the trailing edge is also demonstrated.[13]

The present authors have carried out simulation study of an asymmetric single dielectric barrier plasma actuator[14,15]. They have shown that electron deposition downstream of the overlap region of the electrodes results in formation of virtual negative electrode which always attracts the ions. The force on the charge separation is in positive-x direction during the positive half of the rf voltage and in negative-x direction during negative half of the rf voltage. The magnitude of the former force is higher that the latter. Thus, domain integration of the force on the charge separation and time average of the force was found primarily to be in the positive-x and negative-y direction. In this paper, we study active separation control using asymmetric dielectric barrier plasma actuator. We solve the equations governing dynamics of electrons, ions and fluid to obtain spatio-temporal profiles of electron density, ion density, electric potential, neutral gas density and neutral gas velocity. The parameters controlling the force are the dielectric characteristics, applied voltage, frequency and the asymmetric configuration of the electrodes, thickness of the exposed electrode. The effect of these parameters on separation control is characterized in this paper. In addition, we utilized the force field calculated from the first principles[13] and studied the effect of increasing number of electrodes on the wall jet while the electrodes are kept at a single phase. The momentum transfer to the gas is also predicted for varying the distance between the powered electrodes.

This paper is organized as follows. Section II describes the problem statement. Section III describes and interprets the computed results. Section IV summarizes the conclusions.

II. Problem Statement

Fig. 1 shows schematic of an asymmetric single dielectric barrier plasma actuator. It consists of two electrodes separated by a dielectric. The upper electrode is exposed to the free stream flow while the lower electrode is placed underneath the dielectric. For most of the cases presented here, unless otherwise specified, these two electrodes overlap horizontally with each other. The region simulated is 10 cm long and 5 cm high. The lower part of the domain consists of a 0.1 cm thick insulator with dielectric constant $\varepsilon_d = a\varepsilon_0$ while the upper part is filled with inert helium gas of $\varepsilon_f = 1.0055\varepsilon_0$, where ε_0 is permittivity of the free space. The thickness of the electrodes is assumed to be infinitesimally small. The rf electrode extends from x=0.3 cm to x=1.5 cm at y=0.1 cm, the grounded electrode is from 1.48 cm to 2.75 cm at y=0, with a 0.02 cm overlap between electrodes along the x-axis. The embedded electrode is grounded and a sinusoidal voltage $\phi = \phi_0 \sin(2\pi ft)$ is applied to the exposed electrode. The frequency of excitation is fixed at f =5 kHz.

The initial velocity components u_0 (along the x-direction) and v_0 (along the y-direction) are 10 m/s and 1.75 m/s, respectively, corresponding to an angle of attack (α) of approximately 10 degrees. The separated region observed in the vicinity of the leading edge of the plate is then subjected to control with a suitably placed asymmetric single dielectric barrier plasma actuator.

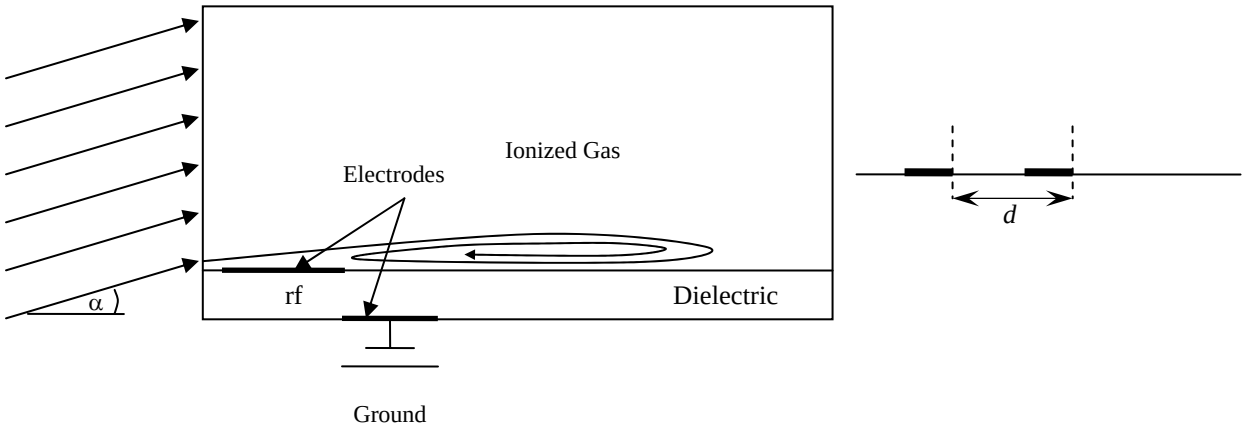

Figure 1. Schematic of an asymmetric single dielectric barrier plasma actuator with an incident gas flow angle α. Single electrode pair on the left and multiple electrode pairs on the right.

The drift-diffusion form of continuity and Poisson's equations for the electrons and ions are solved as described in Ref. 14 together with the following fluid momentum and continuity equations:

$$\frac{\partial n_\alpha}{\partial t} + \nabla(n_\alpha \mathbf{v}_\alpha) = n_e S \text{ , with } n_\alpha \mathbf{v}_\alpha = -\text{sgn}(e) n_\alpha \mu_\alpha \nabla\phi - D_\alpha \nabla n_\alpha \text{ for } \alpha = e, i \quad (1)$$

$$\varepsilon \nabla^2 \phi = e(n_e - n_i), \quad (2)$$

$$\rho \frac{\partial \mathbf{u}}{\partial t} - \nabla(\eta \nabla \mathbf{u}) + \rho(\mathbf{u}.\nabla)\mathbf{u} + \nabla p = e(n_e - n_i)\nabla\phi, \quad (3)$$

$$\frac{\partial \rho}{\partial t} + \nabla(\rho \mathbf{u}) = 0. \quad (4)$$

where n_e, n_i, ρ, $\mathbf{v}_e$, $\mathbf{v}_i$ and $\mathbf{u}$ are densities and velocities of electrons, ions, and the working gas, respectively, η is the gas viscosity, S is the Townsend ionization rate, pressure $p = \rho RT / M$, M (mole/gm) is the molar mass of helium, T is the temperature (300 K), R is the universal gas constant (erg/(mole K)). The bulk density of the helium is taken to be 1.79×10^{-4} gm/cm^3, and the viscosity is assumed to be 1.9 poise. The mobilities μ_α and diffusion rates D_α are taken from Ref. 14. The self-consistent formulation is solved using a Galerkin variational formulation based finite-element method[16] to obtain electron and ion density, electric potential, neutral velocity and density. The no-slip condition is assumed for the gas neutrals at the dielectric surface and the velocity at the left boundary of upper domain is set to the freestream condition at all times. Homogeneous Neumann conditions are applied to the upper edge of the domain. For the charge equations, the total current continuity is ensured across the dielectric interface i.e., at this location, conduction, convection and displacement currents in the gas are balanced with the displacement current in the dielectric.

III. Results and Discussion

We have studied altogether eleven different cases. We have chosen an initial weak ionization of $n_0 = 10^{10}$ /cm^3, a =3.5 (Kapton polyimide), and negligible rf electrode thickness for the reference (base) case. As the gas is preionized, only a small alternating potential of ϕ_0 =400V is applied to the powered electrode. For the other ten cases amplitude of rf voltage ϕ_0, initial plasma density n_0, dielectric constant a, powered electrode shape, the number of electrode pairs and/or the interelectrode streamwise distance are varied to see the influence of these parameters on flow control.

In general, the rf induced plasma actuators work as follows. The electrons are repelled by the insulated electrode and by the exposed electrode during the positive and the negative part of the rf voltage, respectively. The electrons are absorbed at the surface of rf electrode during most of the positive part of the cycle. However, during most of the negative part of the cycle, electrons get deposited at the surface of the dielectric above grounded electrode. The dielectric surface becomes negatively charged. The local imbalance arising from the different mobilities of the ions and

electrons results in a time-varying charge separation distribution and establishment of a consistent electric field. The electric field **E** exerts a net force density $\mathbf{F} = e(n_i - n_e)\mathbf{E}$ on the space charge separated plasma. At all phases in the cycle, the peak magnitude of the force is located downstream of the rf electrode.

Figures 2 (a) and 2 (b) plot the calculated **F** for the base case, as function of ωt at x=1.75 cm and y=0.25 cm and x=2.5 cm and y=0.25 cm, respectively. For Figure 2(a), the x-component of the force takes both positive and negative values during positive and negative parts of the cycle, respectively; its magnitude during the former phase is nearly three times larger than in the latter. The y-component of the force is negative during most of the cycle, becoming marginally positive only at the negative peak of the voltage. Magnitude of both forces is the highest around positive peak of the cycle and almost zero at the end of the cycle. The time average of the force at this point is oriented in the positive x and negative y-direction. Figure 2 (b) shows vector plot of the time average of the force **F**. It can be seen that arrows are directed towards downstream region from both positive-x and negative-x directions. However, the magnitude of positive-x force is much larger than that of negative-x force. The electric field **E** is directed from the rf electrode to grounded electrode and the force on the charge separation also follows the electric lines of force. This explains the things about time average of the force. The plasma is highly collisional which results in energy exchange between charged and neutral species. Consequently, collision effects ensure that the dominant neutral species experience an accelerating body force downstream and towards the dielectric surface. Since fluid cannot penetrate the dielectric, it is turned parallel to the surface of the dielectric. The net effect as discussed further below is therefore a gradual mitigation of flow separation. Ensuring the proper magnitude and direction of the time averaged force is key to successful application of DBD for actuating effect at higher neutral gas speeds.

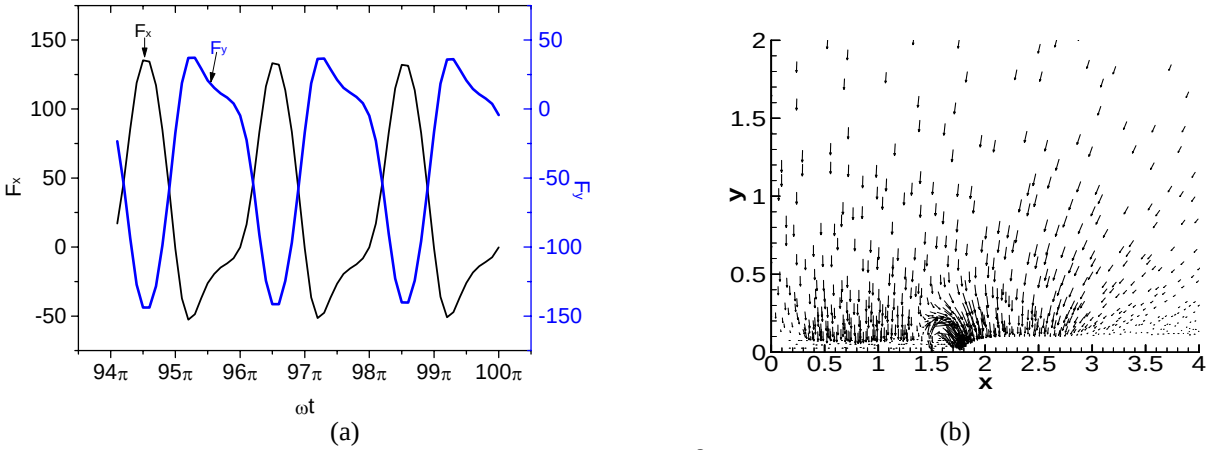

(a) (b)

Figure 2. (a) The force per unit volume $e(n_i - n_e)\mathbf{E}$ (dyne/cm^3) as function of ωt at x=1.75 cm and y=0.25 cm, and (b) Time-averaged force distribution, x and y are in cm.

The effect of the DBD is highlighted by considering the flow field for the base case. The initial field, without plasma actuator, is shown in the first frame of Fig. 3 (a), which depicts the streamline pattern and neutral velocity vector at 1 second (1000 times the characteristic flow timescale) after initiation of the flow. A separation bubble develops near the surface of dielectric – in a practical situation this phenomenon degrades performance through impact on drag or control surface effectiveness. When the plasma actuator is switched on, a highly transient process is initiated as shown in the last three frames of Fig. 3 (a), which depicts streamlines and vectors of neutral velocity after 10, 30, and 50 cycles, respectively. The attachment process downstream of the rf electrode progresses successively downstream: the attachment point is at 6.5 cm after 10 cycles, moving to 8 cm after 30 cycles and finally beyond the computational domain after 50 cycles. This is consistent with the above observation that the net force on the plasma operates downstream of the rf electrode in positive-x direction. The transfer of momentum results in a near-wall energized flow of neutrals, altering the dynamics of the inertial and adverse pressure gradient terms in Eqn. (3) to eliminate the separation bubble. The neutral density is nearly 10^7 times higher than that of the plasma, which is reflected in the time taken to attach the flow over full length of the dielectric. Figure 3 (b) plots the streamwise u-velocity component after 50 cycle parallel to the flat plate for y=0.25 cm, y=0.5 cm, y=1 cm, y=1.5 cm, and y=2 cm. This figure gives us a numerical idea about u-velocity distribution. The u-velocity is nearly zero near the dielectric surface at the end of domain (x=10 cm) and its value increases with the increase y, i.e. as we move away from the dielectric surface.

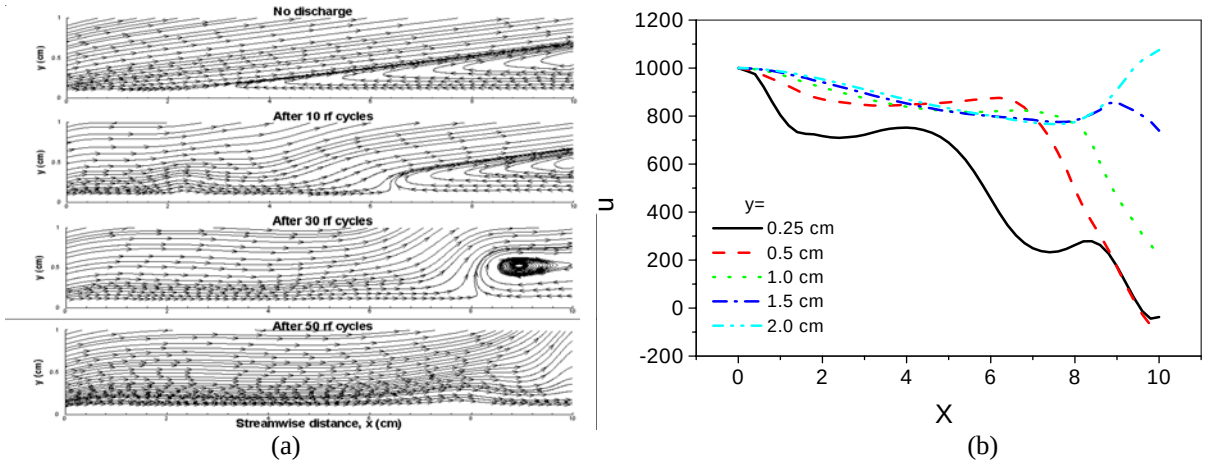

Figure 3. (a) Streamlines and vectors of gas velocity at the end of 1 sec, 10 cycles, 30 cycles and 50 cycles. (b) Streamwise gas velocity component u (in cm/s) after 50 cycles at different height (y) as a function of x (in cm).

The effect of initial plasma density, dielectric constant, excitation potential and rf electrode shape have been explored in Figures 4, 5, 6 and 8, respectively. For each figure, (a) and (b) of each figure show time average of the electrodynamic force density which is the key in flow control, (c) and (d) show arrows and streamlines of weakly ionized gas velocity which are as a consequence of the force operating on the charge separation and give us information about ultimate effect of the force, and (e) and (f) show the streamwise velocity component parallel to the flat plate. The latter shows the momentum transfer due to the force in computational domain.

Figure 4 shows gas plasma interaction for initial plasma density of $n_0 = 5\times10^{10}$ cm^{-3} and 10^{11} cm^{-3} respectively. The higher value of initial density results in larger charge separation and hence higher generated electrostatic field. Consistently, the larger force $e(n_i - n_e)\mathbf{E}$ yields more energetic plasma and neutral velocities. The significant body force component in the –y direction induces downward flow and, due to the wall impermeability, this results in a complex non-linear interaction between the force, inertial and pressure mechanisms. The net result of which is the desired elimination of separation downstream of the electrode.

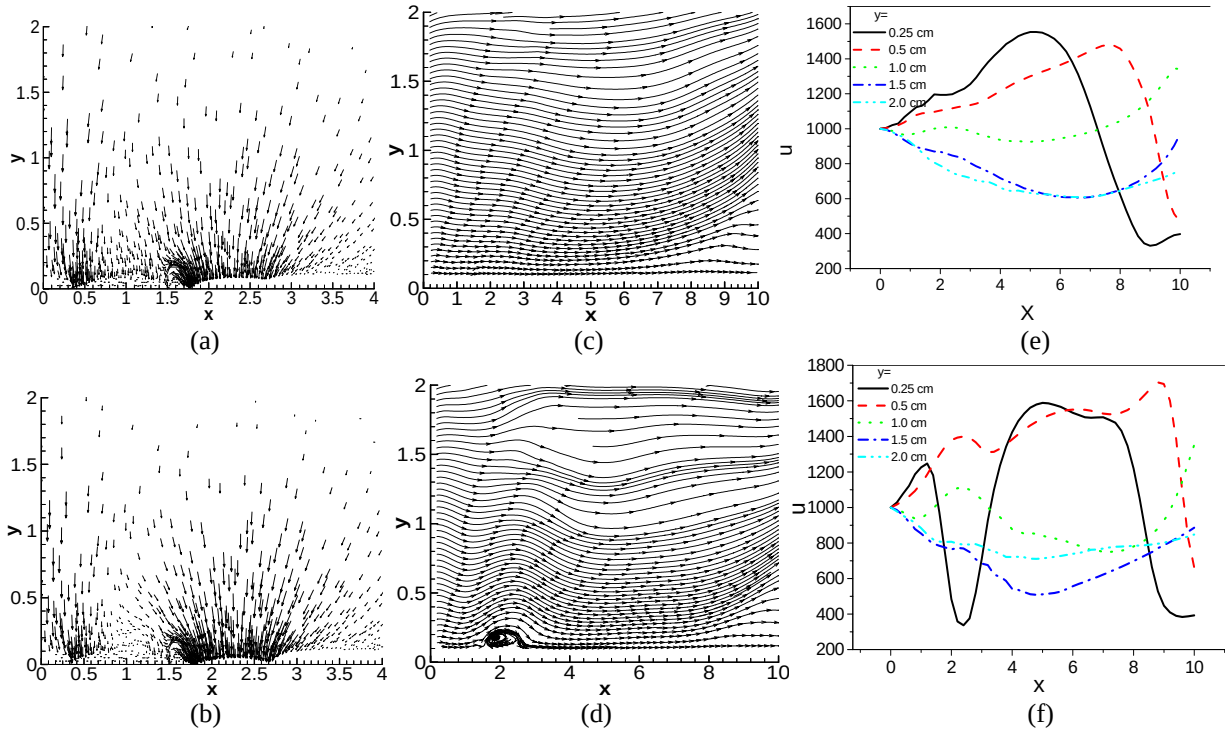

Figure 4. (a) and (b) vectors of time-averaged force distribution, (c) and (d) Streamlines and vectors of gas velocity and (e) and (f) Gas velocity components u (in cm/s) as a function of x for initial plasma density 5×10^{10} /cm^3 and 1×10^{11} /cm^3, respectively. x and y are in cm.

The flow is smoother for initial plasma density of 5×10^{10} /cm^3 than those for initial plasma densities 10^{10} /cm^3 and 10^{11} /cm^3. While the lower force for plasma density 10^{10} /cm^3 is sufficient to eliminate separation bubble nearly as efficiently (see Fig. 3a) as for plasma density 5×10^{10} /cm^3 (Fig. 4c), the force produced for initial plasma density of 10^{11} /cm^3 is larger than required which results in creation of small residual bubble downstream of the rf electrode.

Figure 5 shows arrows of time average of force (a) and (b), arrows of gas velocity (c) and (d) and velocity u as a function of x (e) and (f) for dielectric constant a = 7 and 14, respectively. With the increase in dielectric constant, the magnitude of driver electric field decreases slightly which results in low charge separation and low force on the charge separation. Change in the value of force is not significant therefore small variation of dielectric constant does not have a significant effect on the gas velocities.

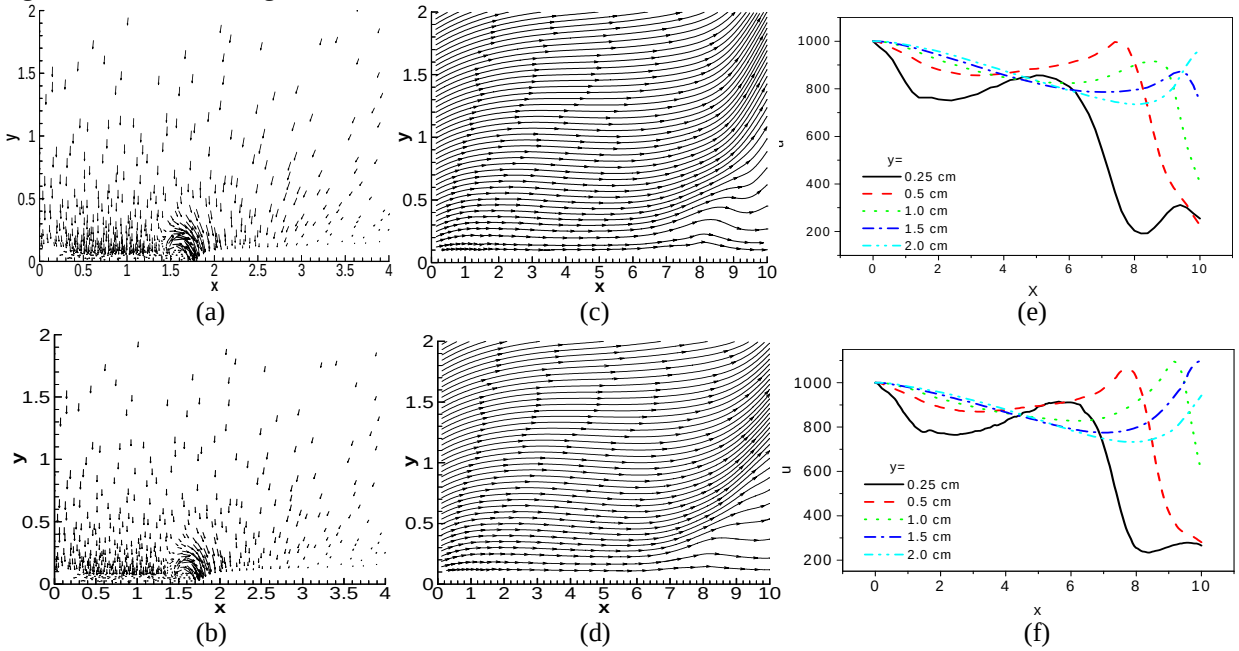

Figure 5. (a) and (b) vectors of time-averaged force distribution, (c) and (d) Streamlines and vectors of gas velocity and (e) and (f) Gas velocity components u (in cm/s) as a function of x for dielectric constant ε =7 and ε =14, respectively. x and y are in cm.

Figure 6 shows results for excitation amplitude ϕ_0 = 300V and 450V, respectively. From the arrow plot of Figs 6 (a) and 6 (b) it can seen that the force is larger for ϕ_0 = 450V case that that for ϕ_0 = 300V case. A low value of excitation amplitude ϕ_0 results in low electric field $\mathbf{E}$ and low value of charge separation $n_i - n_e$ and vice versa. The separation is more effectively eliminated for ϕ_0 = 450V case as the value of force $\mathbf{F}$ is large. A large force results in larger streamwise velocity also. The effect of excitation amplitude has been further explored in Figure 7. Figures 7 (a) and 7 (b) show the time averaged force per unit volume $e(n_i - n_e)\mathbf{E}$ in the x and y directions, respectively as a function of x along y=0.25 cm, while the streamwise velocity component is shown in Figure 7 (c). For all cases, the positive peak of the force is near x=1.75 cm, i.e., just downstream of the trailing edge of the exposed electrode, while negative peak is near x=3 cm. As ϕ_0 increases by 50%, the streamwise force increases by a commensurate amount. The y-component of the force is negative. The magnitude of both the components of the force decrease sharply with y and is negligible beyond x=4 cm. The correlation between velocity and streamwise body force is highlighted in Figure 3(d) which plots them against amplitude of excitation. The figure indicates that the magnitudes of the two quantities are correlated with applied voltage. Showing the relationship u ~ Cϕ_0^m holds (cf. Ref. 6), for u in m/s and ϕ_0 in kV, however, we have determined C = 13.5 and m = 0.5.

Figure 8 shows arrows of time average of force (a) and (b), arrows of gas velocity (c) and (d) and velocity u as a function of x (e) and (f) for finite thickness (0.05 cm) and arcshape rf electrode (x=0.3 to 1.52cm along y=0.1 and 0.2 cm), respectively. The velocities are much higher in the case of arcshape rf electrode case than any other cases reported in this paper. The flow is best attached to the surface in the case of arcshape rf electrode case in Fig. 8 (d) which is due to the increase in the x-component of the force $e(n_i - n_e)\mathbf{E}$. Figs. 8 (a) and 8 (b) demonstrate the effect of electrode radius of curvature. As the curvature increases, the time-averaged force nearly doubles for an arc shaped electrode with a small radius at the tip. This is in agreement with the experimental observation reported in [6] that the force magnitude increases with decreasing radius of electrode. Note the velocity increase for the arc shape in Fig. 8 (f) is extremely high and may be due to numerical overshooting.

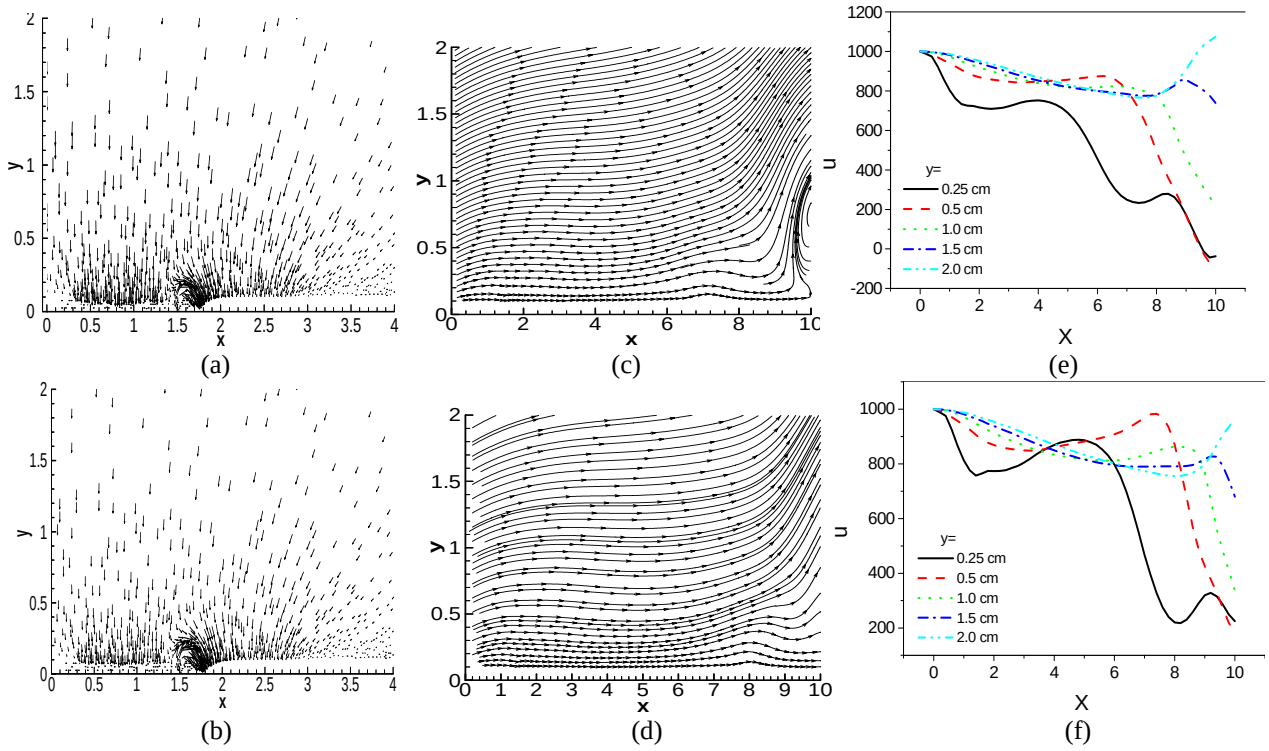

Figure 6. (a) and (b) vectors of time-averaged force F; (c) and (d) Streamlines and vectors of gas velocity; and (e) and (f) Gas velocity components u (in cm/s) for ϕ_0 = 300 volt and ϕ_0 = 450 volt, respectively, x and y are in cm.

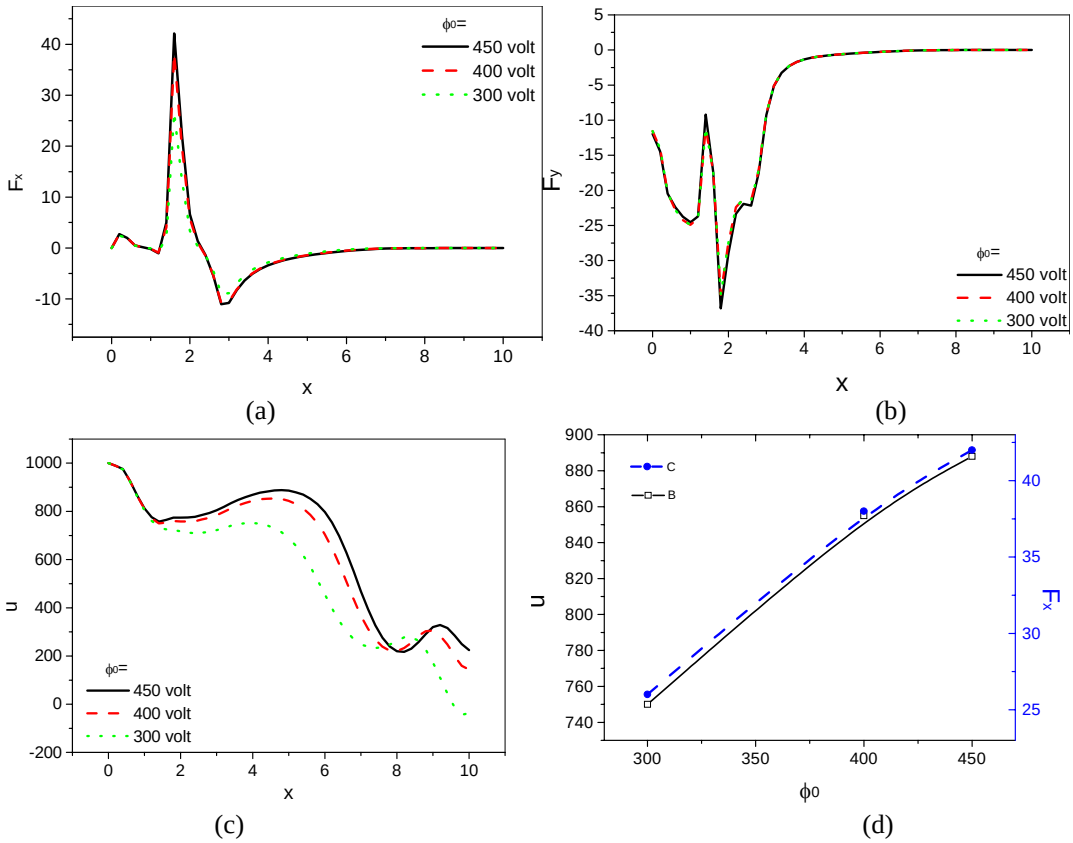

Figure 7. Time average of (a) Fx and (b) Fy the electrodynamic force density and (c) gas velocity (cm/s) as a function of x (in cm) for y=0.25 cm for ϕ_0 =300, 400 and 450V. (d) Streamwise velocity (cm/s) and force F_x (dyne/cm^3) as a function of rf voltage ϕ_0 (in volt).

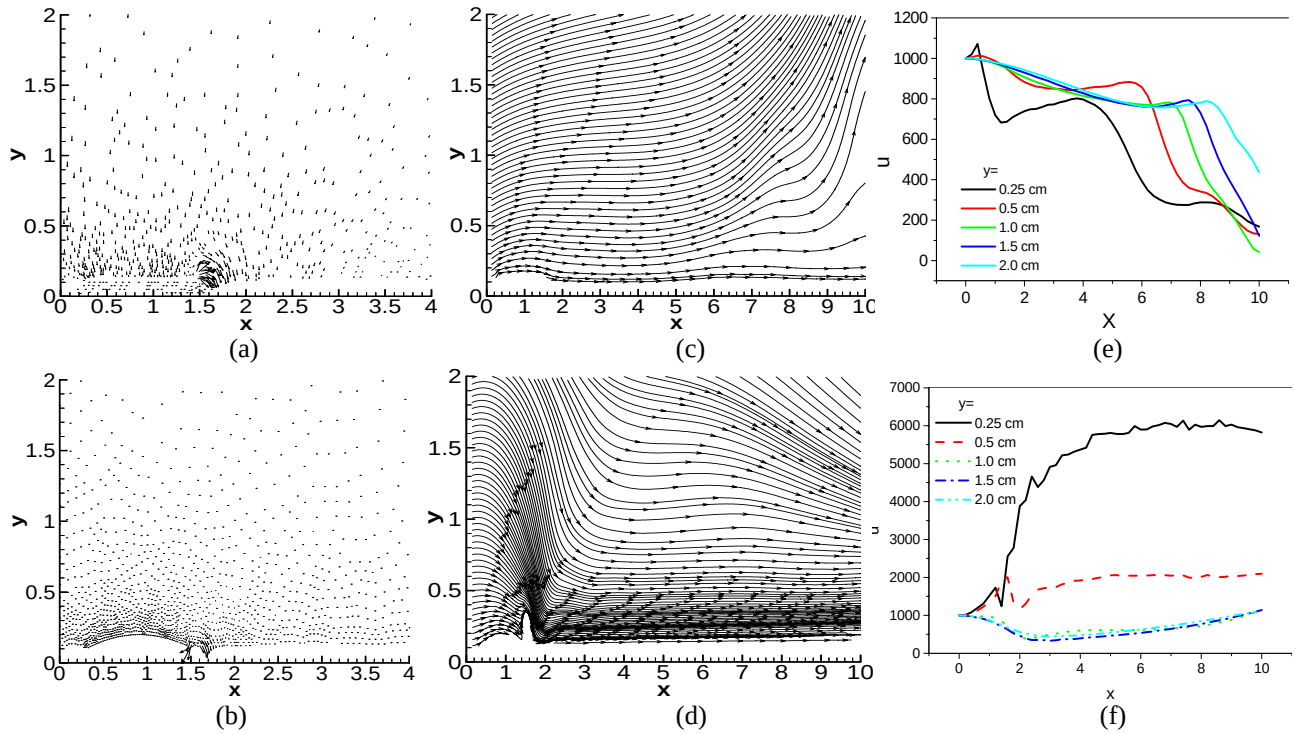

Figure 8. (a) and (b) vectors of time-averaged force distribution, (c) and (d) Streamlines and vectors of gas velocity and (e) and (f) Gas velocity components u (in cm/s) as a function of x for finite electrode thickness (0.05 cm) and arcshape rf electrode, respectively. x and y are in cm.

The effect of frequency and the waveform of the applied rf potential is elucidated in Figure 9. Figs. 9 (a) and 9 (b) show domain integration of streamwise and normal component, respectively, of the force per cm^3 $e(n_i - n_e)\mathbf{E}$ as a function of normalized time for 47th through 50th cycle for ϕ_0 = 300V, 400V, and 500V with initial ionization of n_0 $=10^{11}$ /cm^3 and ϕ_0 = 400V with initial ionization of n_0 $=10^{10}$ /cm^3. Electron deposition downstream of the rf electrode is small and the generated electrostatic field is also small for low density case. Therefore, for n_0 = 10^{10} /cm^3 case, the force follows the rf voltage and it is positive for the positive part of the cycle and negative for the negative part of the cycle. Since the first ionization potential of helium is 24.6 eV, this translates to a reasonably high initial rf amplitude (~kV) for this low preionization. For other cases, the force is positive for all the time except from $\omega t = 98.8\pi$ to $\omega t = 99.2\pi$ and corresponding time points in other cycles. When the cycle changes sign, the electron deposition is at the edge of the rf electrode, and not downstream of the rf electrode. However as the negative cycle progresses, the electrons get deposited downstream of the rf electrode and dielectric surface becomes negatively charged and starts behaving as virtual negative electrode and x-force again becomes positive. Thus, F_x remains positive for most of the cycle. Time average of the force in low density case is two orders of magnitude smaller that that of reference case which is due to 10 times decrease in both charge separation and electrostatic field. With the increase in rf voltage, the amplitude of time average of the x-force slightly increases with a higher shift in the positive direction.

Fig. 9 (b) shows domain integration of F_y as a function of normalized time for 47th to 50th cycle. For n_0 = 10^{10} /cm^3 case, the force follows the rf voltage and it is generally positive for the positive part of the cycle and negative for the negative part of the cycle. For other cases, the force is negative for all the time. Dielectric surface becomes negatively charged and behaves as a virtual negative electrode, therefore, electric field E_y is directed towards dielectric surface. The negative force peaks when the rf voltage is around its positive peak as E_y is strong at this time. With the increase in the magnitude of rf voltage negative magnitude of E_y increases along with the negative magnitude of F_y.

Fig. 9 (c) and 9 (d) shows domain integration of F_x and F_y , respectively, as functions of normalized time between 47th to 50th cycle for sinusoidal f = 1 kHz and f = 25 kHz, and $\phi = \phi_0 \sin^2(\omega t)$ with f = 1 kHz. For 1 kHz case the force follows the rf voltage and it is approximately positive for the positive part of the cycle and negative for the negative part of the cycle. For $\phi = \phi_0 \sin^2(\omega t)$ case, the force is negative when the voltage falls after attaining its peak. The electrons get deposited near the rf electrode during increasing voltage and when the voltage starts falling the area around rf electrode behaves as a cathode and the x-force is negative. The magnitude of the force increases with the increase in the frequency of rf voltage as can be seen from the 25 kHz case. Effect of electrostatic field becomes more prominent with the increase in frequency. The time average of the force is 0.34 dyne/cm^3, 1.18 dyne/cm^3, 2.25 dyne/cm^3

and 1.7 dyne/cm^3, respectively for different cases over the cycles. Fig. 9 (d) shows domain integration of F_y. For 1 kHz case the force follows the rf voltage and it is positive for the positive part of the cycle and negative for the negative part of the cycle. The particles have sufficient time to respond to the applied rf voltage and the effect of electrostatic field does not dominate. For $\phi = \phi_0 \sin^2(\omega t)$ case, largest magnitude of negative force is approximately equal to that for 400 volt case only. It is also similar to 25 kHz and 300 volt cases where force increases with frequency. The time average of the force is 4.36 dyne/cm^3, -34.40 dyne/cm^3, -23.26 dyne/cm^3 and 71.72 dyne/cm^3 respectively for different cases over the cycles.

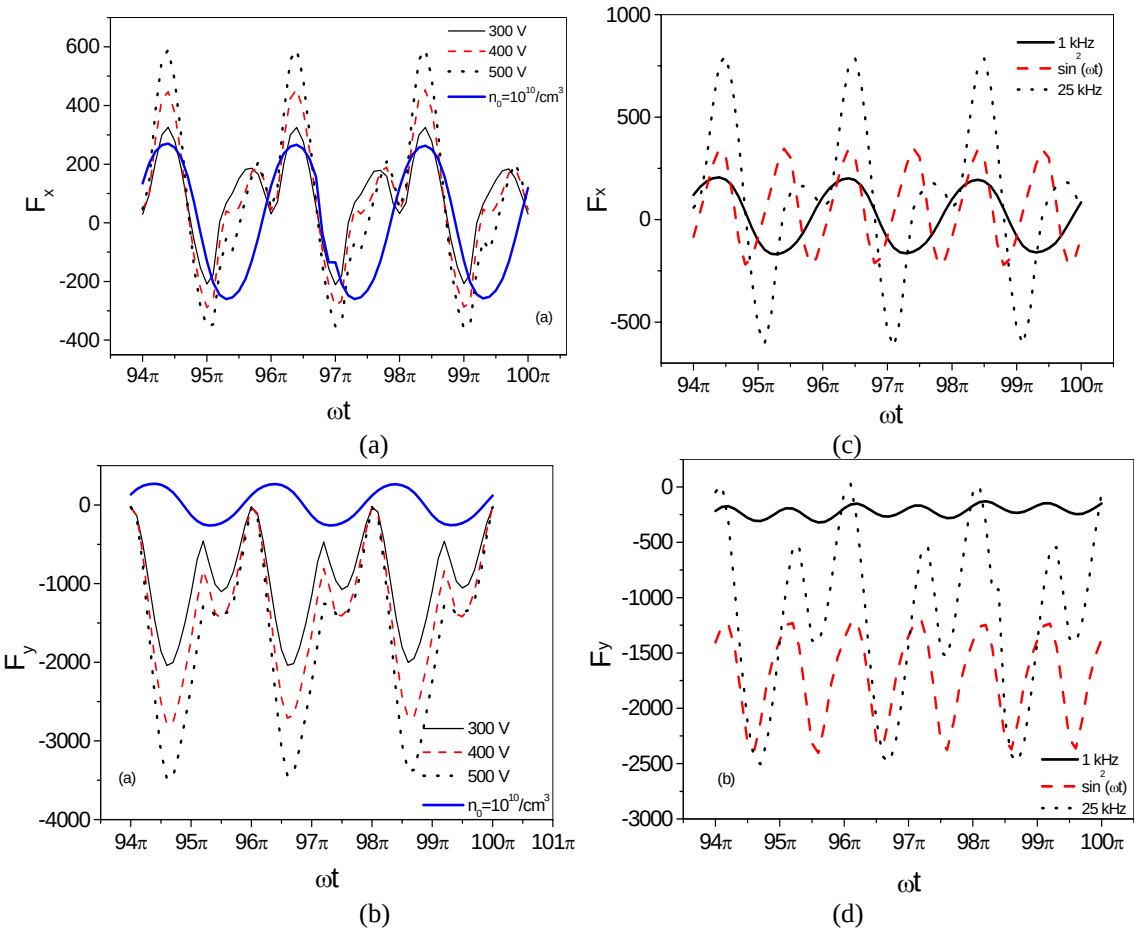

Figure 9. Effect of frequency and waveform on the electrodynamic force components.

Here onwards, the cases presented utilize periodic asymptote force field derived for an asymmetric electrode arrangement from the first principles in Ref. 14. The mass balance equation (4) and gas momentum equation (3) are solved together to generate the velocity field. The effect of forces generated due to plasma formation on free-stream velocity is analyzed for two design parameters in a multiple electrode configuration for fixed electrode length of 3 mm.

First, the streamwise space between the exposed electrodes or inter-electrode gap is varied. The results of velocity distribution in streamwise and transverse directions are shown in Figure 10. We have chosen spacing such that D1=10mm, D2= 6mm, D3= 5mm, and D4= 14mm. The analysis shows that the electrode spacing has a significant effect on the near wall fluid acceleration. Most of force is concentrated in the downstream region of the exposed electrode. Greater the electrode spacing, less effective or less additive is the effect of the force. Any design with gap greater than D1 = 10mm proves to be less effective. The location of the velocity peak gets shifted along y-direction for varying electrode spacing. For example, a seven times rise is observed when probed at downstream location 1mm above the plate. Also, one millimeter reduction of spacing between designs D2 and D3 leads to nearly 21 % increase of peak velocity. Surprisingly, set-up with distances D1 = 10mm and D3 = 5mm exhibit most favorable characteristics compared to D2 = 6mm. Hence, the energy addition to the fluid and consequently the actuator efficiency are dependent on optimizing the design constraint like streamwise inter-electrode gap.

The effect of forces is also analyzed for varying number of electrode pairs maintained at an interelectrode gap of 10mm. The results of velocity distribution are plotted in Figures 11 and 12. A set of forces due to one, two and four pairs of asymmetric electrode configuration is studied. Peak streamwise velocities are at locations just downstream of

the last electrode of any chosen configuration. Three such downstream points are chosen (x1<x2<x3) for every case and compared. It is observed from Figure 11(a) that the near wall fluid velocity increases with number of electrode pairs in the limit of the four-pair configuration studied here. Interestingly, the percentage increase in velocity from a single electrode pair to two-electrode pairs is much prominent (nearly 22% at x2 for example) than configurations with more than two pairs. Only 6% increase is noted at the cost of addition of third electrode pair. Hence, the choice of high number of electrodes for a given plate length may have an effect of diminishing return on flow velocity induced. Figs. 12 (a)-(c) show the velocity vectors for up to four electrode pair configurations. The formation of a localized high velocity zone within few millimeters from the wall (like a wall jet) is clearly noticed here. The vector plots describe the direction and magnitude of the velocity of the flow as a result of the external electric forcing agent. The force contour has a two-dimensional distribution. Hence (apart from the stream-wise velocity addition), the presence of higher number of electrode pair induces small additional transverse momentum downstream of the plate similar to the discussions on Figure 2(b). It may be noticed again that while the peak of the wall jet moves further downstream, the magnitude does not increase significantly with the increase in number of electrodes from two to four. This should be further analyzed using a consistent force and momentum coupling as this gives us critical information about the scale up.

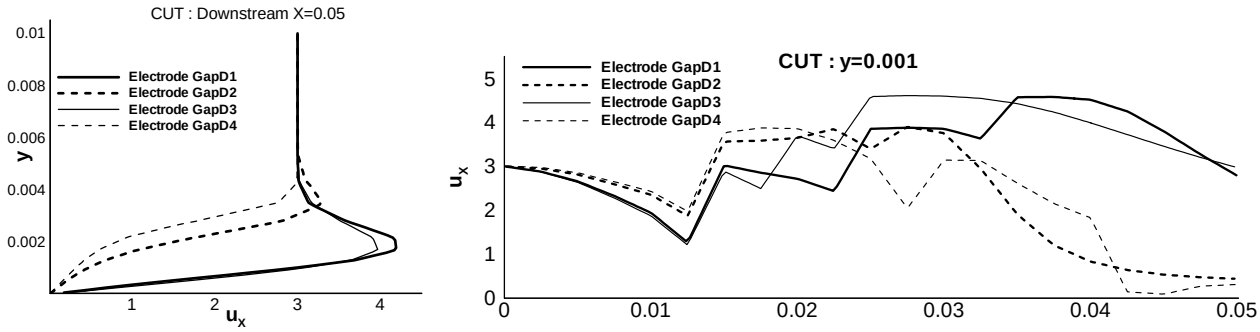

Figure 10. Effect of the distance between electrodes *d* on streamwise velocity. Length of electrode = 3mm, Inter-electrode spacing, *d*: D1=10mm, D2= 6mm, D3= 5mm, D4= 14mm. (a) Along x = 50mm. (b) Along y = 1mm.

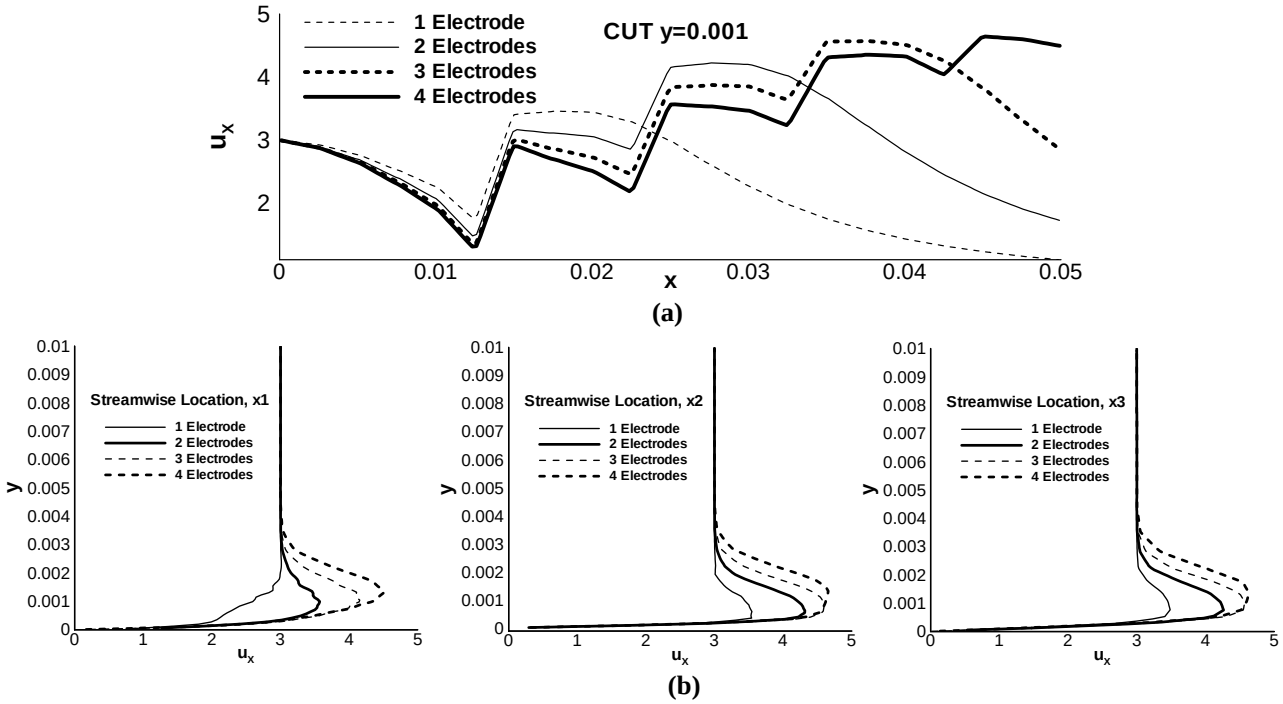

Figure 11. Effect of number of electrodes on the streamwise velocity. (a) Along y = 1mm. (b) Along x measured from the downstream edge of the last exposed electrode : x1 = 0, x2 = 2mm, x3 = 4mm.

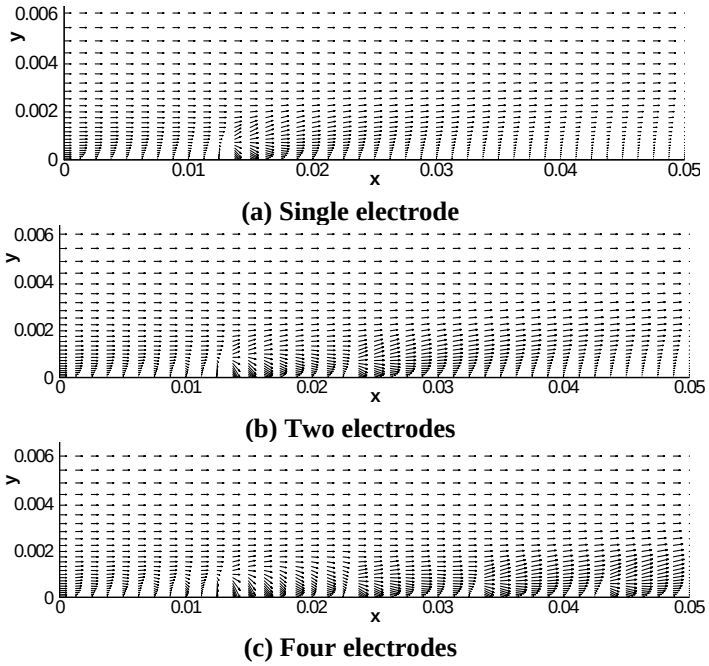

(a) Single electrode

(b) Two electrodes

(c) Four electrodes

Figure 12. Velocity vectors show effect of the number of electrodes.

IV. Conclusions

Separation control using an asymmetric dielectric barrier plasma actuator has been studied by considering the neutral gas flow past a flat plate at an angle of attack. A self-consistent plasma actuator model is employed to study effect of different parameters on separation control. The model is applied to simulate an atmospheric surface dielectric barrier discharge for partially ionized helium gas. The equations governing dynamics of electrons, ions and neutrals are solved using a two-dimensional finite element based formulation of plasma–fluid interactions to study separation control for different parameters. The electric field generated due to charge separation is governed by Poisson equation. The electrons and ions in opposite directions move due to applied driver rf potential. Dielectric surface becomes negatively charged due to electron deposition and starts behaving as a virtual negative electrode for a part of cycle. A time averaged force, predominantly downstream with a transverse component towards the wall, acts on the plasma, which results enhancement of near-wall momentum of neutral gas that effectively eliminates the separation bubble. The computed results are similar to the experimental data. The effect of the amplitude of excitation, dielectric constants, the initial ionization level, and the electrode shape is determined for the effectiveness of plasma actuators. In addition, the electrodynamic body force computed from the first principles is used to study the effect of the number of electrodes on the wall jet while the electrodes are kept at a single phase. The prediction shows significant increase of streamwise velocity for two electrode pairs compared to a single electrode pair. However, for increasing number of the electrodes a diminishing return is observed. The momentum transfer to the gas is also predicted for varying streamwise distance between the powered electrodes. For the two electrode pair setup, an optimum distance exists where maximum momentum is transferred. More investigation is needed to ascertain optimum electrical parameters. In the near future, the model will be extended to multiple actuators with air-with negative ions and additional new mechanisms in the source terms. A model for realistic fully three-dimensional geometric and electrode configuration is also under development, as is an exploration of the effect of different voltage waveforms. The present effort thus provides a practical tool to augment experimental observations in exploring flow control concepts and in developing suitable inputs for traditional fluid dynamics codes based on the Navier-Stokes equations.

Acknowledgements

This work was partially supported by the AFOSR grant no. FA9550-05-1-0074 monitored by John Schmisseur and the Air Force Research Laboratory contract no. F33615-98-D-3210 and the National Academy of Science NRC/AFOSR research fellowship during the summer of 2004. The authors acknowledge many thoughtful discussions with Jonathan Poggie.

References

[1] R.E. Mayle, J. Turbomachinery **113** 509, (1991).
[2] K.W. Van Treuren, *et al.* J. Turbomachinery **124,** 100 (2002).
[3] J.P. Bons, R. Sondergard and R.B. Rivir, J. Turbomachinery **123,** 198 (2001).
[4] L.S. Hultgren and D.E. Ashpis, Bull. Amer. Phys. Soc. **47**, No. 10, 167 (2002).
[5] J.R. Roth, Phys. Plasmas **10**, 2117 (2003).
[6] C.L. Enloe, *et al*., AIAA J. **42**, 595 (2004).
[7] C. Baird, C.L. Enloe, T.E. McLaughlin and J.W. Baughn, AIAA-2005-0565, 43rd Aerospace Sciences Meeting, 2005, Reno, Nevada.
[8] T.C. Corke and M.L. Post, AIAA-2005-0563, 43rd Aerospace Sciences Meeting, 2005, Reno, Nevada.
[9] G.I. Font, 40th AIAA/ASME/SAE/ASEE Joint propulsion conference and Exhibit, July, 2004, Fort Lauderdale, Florida.
[10] S. Roy and D.V. Gaitonde, AIAA-2005-0160, 43rd Aerospace Sciences Meeting, 2005, Reno, Nevada.
[11] S. Roy and D.V. Gaitonde, AIAA-2005-4631, 35th AIAA Fluid Dynamics Conference and 36th AIAA Plasma Dynamics and Lasers Conference, Toronto, Canada, June 2005.
[12] D.V. Gaitonde, M.R. Visbal and S. Roy, AIAA-2005-5302, 36th AIAA Plasmadynamics and laser coferance, June 2005, Toronto, Canada.
[13] D.V. Gaitonde, M.R. Visbal and S. Roy, AIAA-2006-1205, 44th Aerospace Sciences Meeting, 2006, Reno, Nevada.
[14] S. Roy, Appl. Phys. Lett. **86**, 101502 (2005).
[15] K.P. Singh and S. Roy, J. Appl. Phys. **98**, 083303 (2005).
[16] S. Roy, et al., Phys. Plasmas, **10**, 2578 (2003).